Z. Phys. B – Condensed Matter 71, 237–246 (1988)

Condensed Matter
Zeitschrift für Physik B

Quantization of Hénon's map with dissipation II – numerical results

R. Graham[1], S. Isermann[1], and T. Tél[2]

[1] Fachbereich Physik, Universität-GHS-Essen, Federal Republic of Germany
[2] Institute for Theoretical Physics, Eötvös University, Budapest, Hungary

Received November 26, 1987

The master equation for a quantized version of Hénon's map with dissipation derived in a preceding paper is here solved numerically for the Wigner quasi-probability density, under conditions of period doubling and classical chaos both in the transient regime and in the dissipative steady state. Approximations of the quantum map by a classical stochastic process are also considered and compared with solutions incorporating non-classical quantum fluctuations.

1. Introduction

The study of quantum effects in classically chaotic systems continues to be a very active field of research [1]. While a large number of results on conservative quantum systems is by now available, results on dissipative quantum systems are still rather sparse, even though it is widely appreciated that *(i)* dissipative effects in many quantum systems are non-negligible, and *(ii)* that some quantum effects are very sensitive to small perturbations with dissipation.

In a preceding paper [2] (henceforth quoted as I) two of us have considered a dissipative system (a nonlinearly kicked damped harmonic oscillator) which is classically described by a two-dimensional discrete map of the type first introduced by Hénon [3]. After a suitable choice of parameters these maps, numerically, show behavior indicating the existence of a strange attractor. Quantum mechanical master equations describing quantized versions of these maps have been derived in I and were used there to obtain analytical asymptotic results for the quantum corrections to classical behavior in the limit $\hbar \to 0$. The present paper is a sequel to I, and has the purpose to present more detailed numerical solutions of one of the master equations derived in I. Numerical results for the quantized standard map with dissipation [4] have been reported in [5]. A part of the original results of the present paper has been reviewed in [6], together with further results on dissipative quantum maps.

The paper is organized as follows. In Sect. 2 we summarize the necessary results of I concerning the dissipative quantum map we wish to analyze. Section 3 gives some results for the classical attractor and the phase space density it supports. Iterations of the map, for the effective $\hbar$ rather deep inside the quantum regime, from an initial state into the final steady state are then considered in Sect. 4. In Sect. 5 the Wigner distribution in the steady state for small values of the effective $\hbar$ is considered and compared with a classical stochastic approximation which is exact asymptotically for $\hbar \to 0$. In Sect. 6 we return to the problem of relaxation to the steady state and numerically determine the longest lived transient component of the Wigner distribution and its decay rate. We close, in Sect. 7, with some results for the Wigner distribution in the period doubling regime.

2. The dissipative quantum map

We wish to study a quantum version of a classical two-dimensional map of the form

$$\begin{aligned} x_{n+1} &= f(x_n) - b\, y_n \equiv x^0(x_n, y_n) \\ y_{n+1} &= x_n \equiv y^0(x_n, y_n) \end{aligned} \tag{2.1}$$

first introduced by Hénon. Here the parameter b ($0 < b < 1$), $b = 0.3$ in the following) gives the Jacobian of the map and therefore describes dissipation. The function $f(x)$ chosen by Hénon was $f(x) = 1 - ax^2$, which turns (2.1) into a minimal 2-dimensional generalization of the logistic map. For our purposes this particular choice has the undesirable feature that part of the (x, y)-plane is attracted to infinity under itera-

tions of the map. Classically, difficulties with this can be avoided by starting initially only with points outside the domain of attraction of ∞. However, quantum mechanically there will always be some tunnelling between the domains of different attractors, and therefore, the existence of an attractor at ∞ always renders the total system unstable. In the following, we therefore make the choice

$$f(x)=1-\frac{ax^2}{1+x^4} \tag{2.2}$$

which avoids this problem.

Next, we proceed from the classical map (2.1) to a quantum mechanical master equation. This can be done by recalling that (2.1) is the stroboscobic map of a nonlinearly kicked damped harmonic oscillator. (We shall normalize the unperturbed frequency of this oscillator to be $\omega=1$.) The damping of the oscillator can be modelled by coupling the conservative oscillator to a reservoir of many other harmonic oscillators and subsequently eliminating the reservoir oscillators in Markov approximation. These steps were carried out in I, to which the reader is referred for details. The result of this procedure is a master equation ((3.4) of I) governing the time evolution of von Neuman's statistical operator ρ describing the mixed state of the kicked damped oscillator. The statistical operator ρ is most conveniently, and completely generally, represented by Wigner's quasi-probability density $W(x,p)$

$$\begin{aligned} W(x,p)&=\int\frac{\mathrm{d}q}{2\pi\hbar}\mathrm{e}^{-\frac{\mathrm{i}pq}{\hbar}}\left\langle x+\frac{q}{2}\right|\rho\left|x-\frac{q}{2}\right\rangle \\ \rho&=\int\mathrm{d}p\int\mathrm{d}q\mathrm{e}^{\frac{\mathrm{i}pq}{\hbar}}\int\mathrm{d}x\left|x+\frac{q}{2}\right\rangle W(x,p)\left\langle x-\frac{q}{2}\right|. \end{aligned} \tag{2.3}$$

While x directly corresponds to x in the classical map (2.1) the momentum variable p corresponds to the variable y in (2.1) via

$$p=-\sqrt{b}\,y+\frac{f(x)}{\sqrt{b}}. \tag{2.4}$$

(In I the variable y was defined with a different scale factor which corresponds to replacing $\sqrt{b}\,y\to y$ in (2.4) and all other equations.) In the representation (2.3) with y defined by (2.4) the master equation derived in I takes the explicit form (cf. (4.8), (4.9) of I, where we put $\omega=1$)

$$W_{n+1}(x,y)=\int\mathrm{d}x'\,\mathrm{d}y'\,K(x,y;x',y')\,W_n(x',y') \tag{2.5}$$

with

$$\begin{aligned} K(x,y;x',y')&=\frac{1}{\sqrt{2\pi\hbar Q}}\exp\left[-\frac{1}{2\hbar Q}(x-x^0(x',x'))^2\right] \\ &\cdot\int\frac{\mathrm{d}\eta}{2\pi}\exp\left[-i\eta(y-y^0(x',y'))-\frac{hQ}{2b}\eta^2+iG(x,\eta,\hbar)\right] \end{aligned} \tag{2.6}$$

and

$$G(x,\eta,\hbar)=\frac{1}{\sqrt{b}\hbar}\left[\int_{x-\frac{\eta\hbar}{2\sqrt{b}}}^{x+\frac{\eta\hbar}{2\sqrt{b}}}f(\xi)\,\mathrm{d}\xi-\frac{\eta\hbar}{\sqrt{b}}f(x)\right] \tag{2.7}$$

$$Q=\frac{1-b}{2}\coth\left(\frac{\hbar\omega}{2k_BT}\right). \tag{2.8}$$

Equation (2.6) shows how the classical map (2.1) is built into the quantum map via the functions $x^0(x,y)$, $y^0(x,y)$ defined in (2.1). Equation (2.8) shows how the quantum mechanical form of the fluctuation dissipation relation determines the noise intensity Q at the reservoir temperature T which appears as a width in the kernel of (2.6). In the numerical work of this paper we shall always assume that $k_BT\ll\hbar\omega$, in which case we may replace (2.8) by $Q=(1-b)/2$. We note that even in the absence of dissipation, i.e. for $b=1$, where Q vanishes, the kernel (2.6) still has a finite width which is generated by the function G of (2.7), i.e. by the nonlinearity of the function $f(x)$ appearing in the map (2.1). In the following it will be useful to expand the expression (2.7) as a power series in $\hbar\eta$

$$G(x,\eta,\hbar)=\frac{\hbar^2\eta^3}{4b^2}\cdot\frac{f''(x)}{6}\cdot\left(1+O\left(\frac{\hbar^2\eta^2}{b}\right)\right). \tag{2.9}$$

In our numerical work, for the values of $\hbar, b$ and Q which we shall use, the terms of order $\left(\frac{\eta\hbar}{\sqrt{b}}\right)^4$ not written explicitly in (2.9) will be entirely negligible in (2.6), i.e. it will be safe to use the leading term of (2.9) instead of the full but more complicated expression (2.7).

Then, the η-integral in (2.6) can be carried out and we arrive at the more explicit form of the kernel ((5.3) of I)

$$\begin{aligned} K(x,y;x',y')&=\frac{1}{(2\pi\hbar Q)^{1/2}}\left(\frac{8\sqrt{b}}{\hbar^2|f''(x)|}\right)^{1/3} \\ &\cdot\exp\left[-\frac{1}{2\hbar Q}(x-x^0(x',y'))^2\right] \\ &\cdot\exp\left[\frac{16Q^3b}{3\hbar(f''(x))^2}+\frac{4Qb}{\hbar f''(x)}(y-y^0(x',y'))\right] \\ &\cdot\mathrm{Ai}\left(\left[y-y^0(x',y')+\frac{2Q^2}{f''(x)}\right]\left(\frac{8b^2}{\hbar^2f''(x)}\right)^{1/3}\right). \end{aligned} \tag{2.10}$$

Here $\mathrm{Ai}(x)$ is the Airy function, which falls off rapidly (like $x^{-1/4}\exp(-2x^{3/2}/3)$) for positive x but oscillates like $|x|^{-1/4}\cdot\cos(2|x|^{3/2}/3-\alpha)$ for negative x. It should be noted, however, that the exponential prefactor of the Airy function in (2.10) tends to suppress its oscillatory regions while it enhances its regions of monotonic behavior. These mutually counteracting influences in (2.10) describe the competition between quantum mechanical coherence effects (oscillations of the Airy function) and dissipative effects (suppression of oscillations).

3. Classical results

First we consider the bifurcation diagram of the classical map (2.1) for $b=0.3$ in the domain of the control parameter $a\in[0, 5]$. To generate the diagram shown in Fig. 1, 100 randomly picked initial points $(x, y)\in[-2, 2]\times[-2, 2]$ were iterated 100 times in order to converge on the attractors of the map and the x coordinates of the following iterates were then plotted. This was repeated for 500 evenly spaced values of a covering the chosen interval. The bifurcation diagram has the typical structure (fixed point, period doubling, chaos, periodic windows) known for Hénon's map with quadratic nonlinearity. In the following a fixed value $a=3.4$ is chosen, where, numerically, the map has a strange attractor.

In Fig. 2 the attractor is generated globally in the x, y plane by plotting 2000 iterates, again discarding transients by dropping the first 100 iterates. Figure 3a–d gives increasing local amplifications (by factors 100, respectively) of the substructure of the strange attractor inside the square shown in Fig. 2.

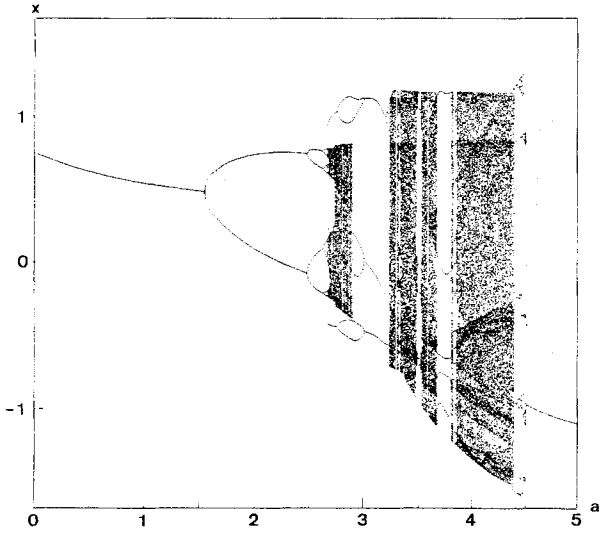

Fig. 1. Bifurcation diagram of the map (2.1), (2.2) for $b=0.3$

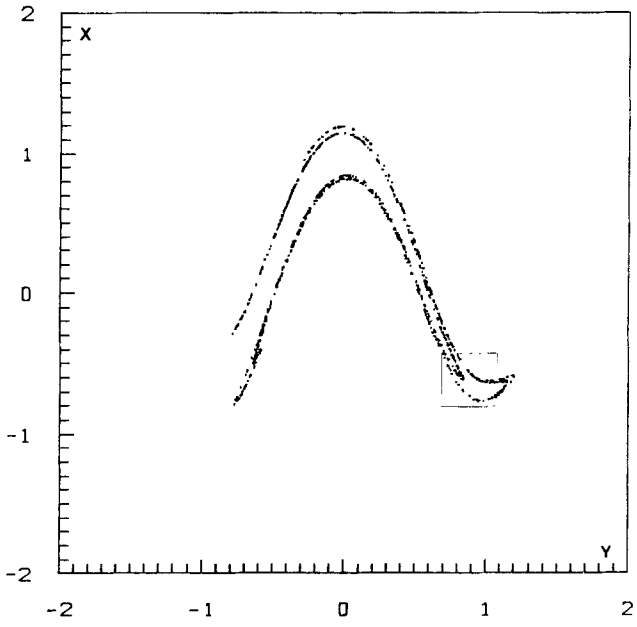

Fig. 2. 2000 non-transient iterates of the map (2.1), (2.2) for $a=3.4$, $b=0.3$

In order to maintain a number of 10^3 points per diagram the number of iterations was increased up to 1.7×10^7.

Next we wish to construct the classical phase-space probability density which is supported by the attractor of Fig. 2. The following procedure proved to be very stable and efficient. The interval $(x, y)\in[-l, l]\times[-l, l]$ is partitionned into squares as shown in Fig. 4 for the example of $l=2$ and the partition is then mapped by applying (2.1). The result is also shown in Fig. 4. Lines of $x=$const. are mapped on lines $y=$const. by (2.1), while lines $y=$const. are mapped onto the curves

$$x=1-\frac{ay^2}{1+y^4}-b\cdot\mathrm{const} \tag{3.1}$$

shown in Fig. 4. The mapping of the squares in the lower right corner is also indicated there, as an example. We wish to choose l such that the mapped partition lies inside the original partition, which requires

$$l>\max\left[\frac{1}{1-b}, \frac{a/2-1}{1-b}\right]. \tag{3.2}$$

Then each point within the chosen square eventually (for $n\to\infty$) must land on the attractor. It is clear from (3.2) that close to the conservative limit $b\to1$ the square must become very large, i.e. this limit is not covered by the following procedure. In the numerical work of this paper we always choose $b=0.3$. Next,

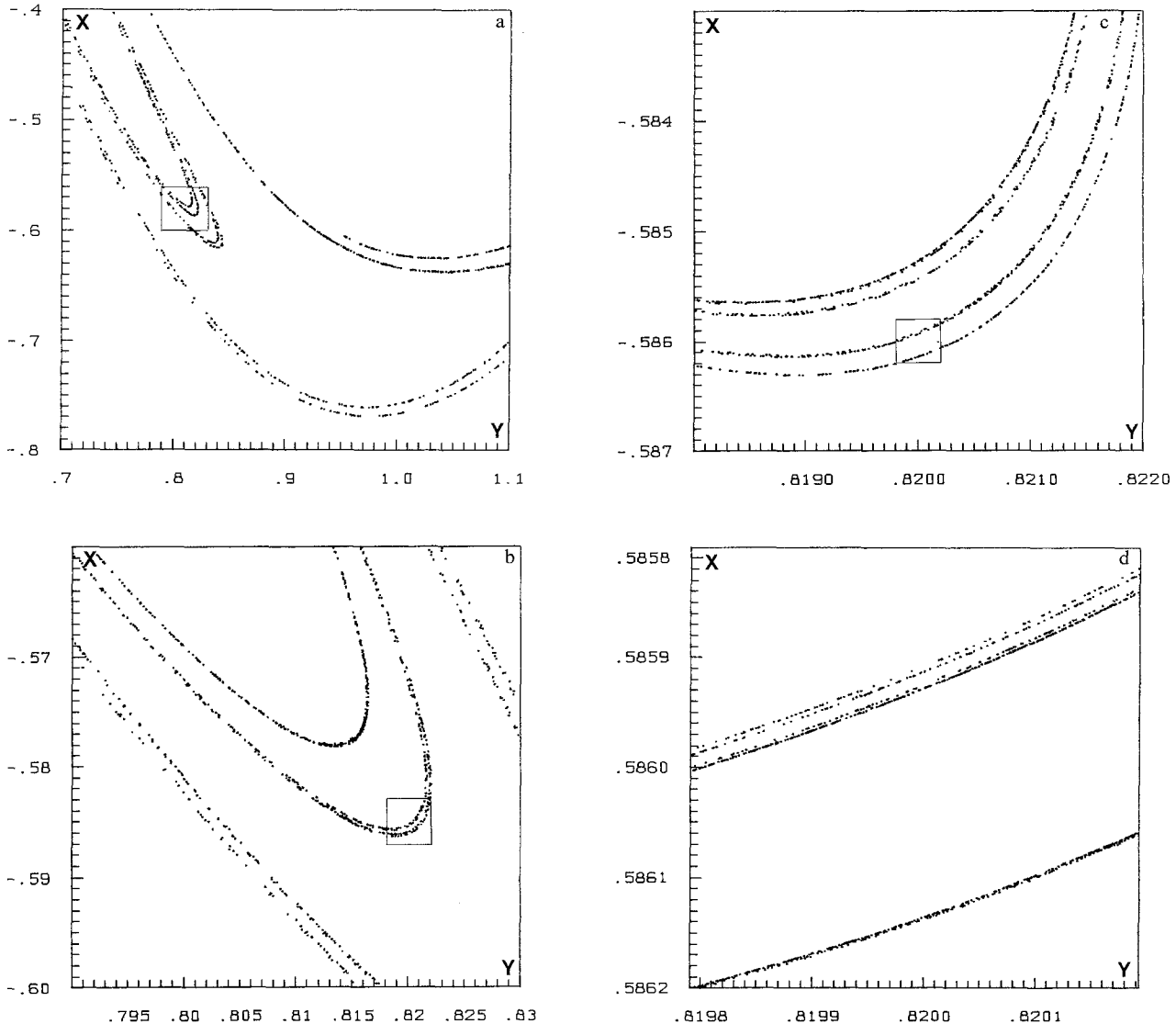

Fig. 3a–d. Increasing local amplification of the square shown in Fig. 2, increasing the number of iterates to generate 10^3 points per plot

the area of the mapped partition inside each of the squares of the original partition is computed. This procedure is used to generate a positive matrix p_{ij} which gives the fraction of the area of the square labelled by j which is mapped into the square labelled by i. Clearly $\sum_i p_{ij}=1$ by definition. Iterating the action of this matrix on any initial distribution W_i over the squares of the partitition until convergence is achieved one generates a stationary distribution $W_{\infty i}$

$$W_{\infty i}=\lim_{n\to\infty}\sum_j (p^n)_{ij} W_j \tag{3.3}$$

which approximates the stationary phase space density for sufficiently fine partitions.

In Fig. 5 we show the result obtained in this manner with $n=50$ for a partition with $l=2$ and 10^4 squares. Only the grossest features for the substructure shown in Fig. 2 are resolved within the chosen partition. The pronounced 3-peak structure of the probability density on the attractor indicates that, for the chosen values of a, b the system is chaotic but close to a 3-cycle, which is also visible in Fig. 1.

4. Transient Wigner distribution

The numerical method for the classical case described in the preceding section must now be generalized to the quantum domain. In doing this we wish to maintain for our calculations the convenience and efficiency introduced by the partition of the phase space

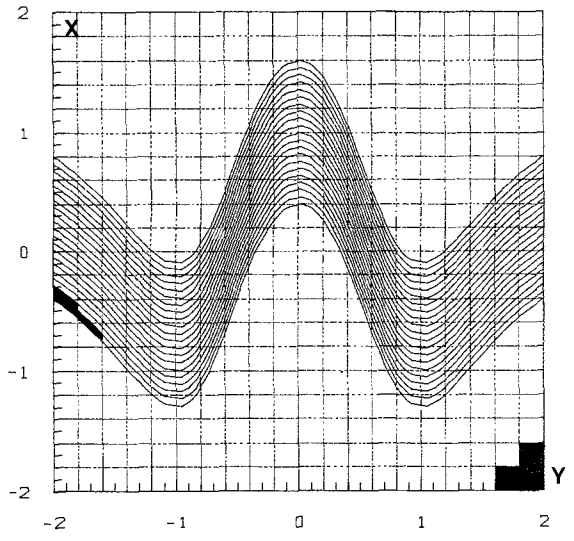

Fig. 4. Partition of the (x, y)-plane and its image under the map (2.1), (2.2) for $a=3.4$, $b=0.3$

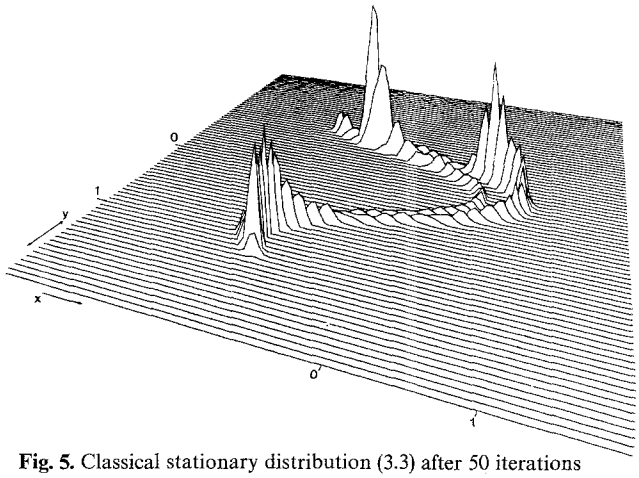

Fig. 5. Classical stationary distribution (3.3) after 50 iterations

into a grid of squares. The form in which the kernel (2.6) incorporates the classical map lends itself to represent (2.6) on the partition by

$$K(x_i, y_i; x'_j, y'_j) \equiv K_{ij} \tag{4.1}$$

$$K_{ij} = \sum_k G_{ik} p_{kj} \tag{4.2}$$

where p_{kj} is the classical transition matrix introduced in the preceding section and

$$G_{ik} = \frac{1}{\sqrt{2\pi\hbar Q}} \exp\left[-\frac{1}{2\hbar Q}(x_i - x_k)^2\right] \cdot \int \frac{d\eta}{2\pi} \exp\left[-i\eta(y_i - y_k) - \frac{hQ\eta^2}{2b} + iG(x_i, \eta, \hbar)\right] \tag{4.3}$$

describes all quantum effects. In (4.1) (x_i, y_i) are the coordinates of the midpoint of the square labelled by i. Furthermore, we assumed that the function G_{ik} is constant, to sufficiently high accuracy, as a function of x_i, y_i within a single square of the partition. This assumption and our goal to observe quantum effects in the Wigner distribution imposes an upper limit on the tolerable size of the squares used in the partition. The minimal quantum uncertainty $\Delta x \cdot \Delta y = \hbar/2\sqrt{b}$ should be much larger than the area of a single square. With decreasing values of $\hbar$ we therefore use correspondingly finer partitions. In the present section we begin by considering the transient relaxation of an initial state to the final steady state for a rather large value of the effective $\hbar$, namely $\hbar = 0.1$. The partition is made by dividing the square $|x|, |y| < 2.5$ into 10^4 squares. The initial state we choose to be localized around $x=0$, $y=0$, and we assume

$$W_0(x, y) = \frac{1}{2\pi\sigma^2} \exp\left(-\frac{x^2+y^2}{2\sigma^2}\right). \tag{4.4}$$

In order to satisfy the inequality

$$\mathrm{Tr}\,\rho^2 \leqq 1 \tag{4.5}$$

i.e.

$$\int dx \int dy\, W^2(x, y) \leqq \frac{\sqrt{b}}{2\pi\hbar} \tag{4.6}$$

the inital state must satisfy

$$\sigma^2 \geqq \frac{\hbar}{2\sqrt{b}}. \tag{4.7}$$

In the following we choose $\sigma^2 = 0.5$ in accordance with (4.7). In Fig. 6a–c the initial state and its first two iterates are shown, Fig. 6d shows the converged steady state, which is reached after about 4 iterations. The rather large value of the effective $\hbar$ leads to a practically complete obliteration of the classical attractor in the steady state by the strong quantum noise. Quantum effects are also visible by the negative values which the Wigner distribution attains in some parts of phase space. In the computations, the large quantum fluctuations caused a practical difficulty by the fact that the Wigner distribution did not vanish to sufficient accuracy on the boundaries $|x| = 2.5$, $|y| = 2.5$ of the square to which the calculations were restricted. This difficulty was resolved by closing the square into a torus, which has some effect – but not a drastic one – on the form of the distributions shown in Fig. 6.

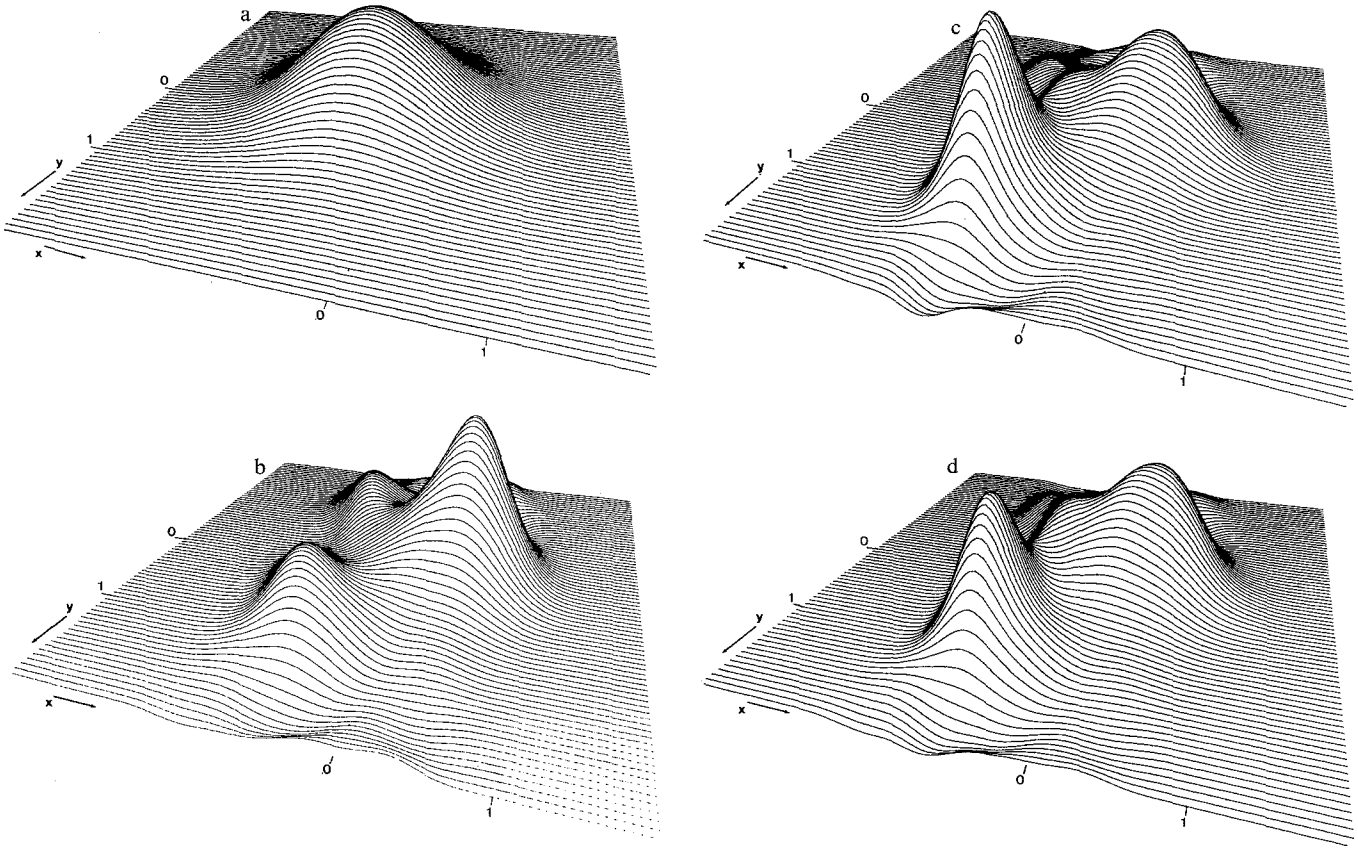

Fig. 6. a initial state (4.4); **b, c** its first two iterates under the map (4.2); and the steady state (6 iterations) **d** for $a=3.4$, $b=0.3$, $\hbar=0.1$

5. Wigner distribution in the steady state

Now we concentrate on the steady state and consider the Wigner distribution for smaller values of the effective $\hbar$. In Fig. 7 we show the Wigner distribution for $\hbar=0.01$ and a partition of the phase space $(x, y)\in[-2, 2]\times[-2, 2]$ into 10^4 squares. The substructure of the classical attractor now begins to show up in the quasi-probability density. Negative values of the Wigner distribution are seen to arise on the concave sides of the classical attractor. These negative values occur because of the oscillations in the Airi function in (2.10) which, in turn, are caused by the function $G(x, \eta, \hbar)$ represented by (2.9). Other features visible in Fig. 7 are a still considerable broadening of the quasi-probability density transverse to the attractor but also a pronounced smoothening of the distribution longitudinal to the classical attractor. The latter effect is apparent if Fig. 7 is compared with the classical distribution of Fig. 5, and it is easily understood as a consequence of the exponential instability of the classical map in the direction parallel to the attractor. For sufficiently small $\hbar$ the function $G(x, \eta, \hbar)$ in (2.6), being proportional to $\hbar^2$, becomes

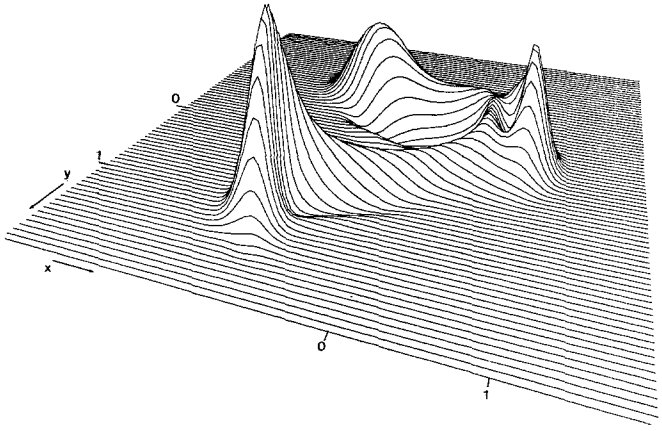

Fig. 7. Stationary Wigner distribution (20 iterations) for $a=3.4$, $b=0.3$, $\hbar=0.01$

negligible compared to the term $\hbar Q\eta^2/2b$ in the exponent of the η-integrand in (2.6). Dropping this term completely we obtain the approximate Wigner distribution shown in Fig. 8, which lacks the negative parts of the Wigner distribution in Fig. 7 but is otherwise an excellent approximation to Fig. 7. This approxi-

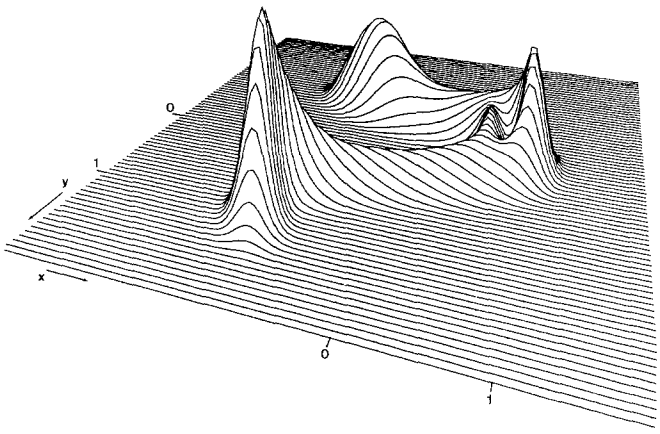

Fig. 8. Stationary Wigner distribution (20 iterations) for Gaussian approximation for the quantum noise for $a=3.4$, $b=0.3$, $\hbar=0.01$

mation must improve for decreasing values of $\hbar$. In Fig. 9a and b we compare for the case $\hbar=0.001$ the stationary Wigner distributions obtained with and without including the G-function in (2.6) and notice that the results coincide within the accuracy of the drawing. These results were obtained for a partitioning of the square $(x, y)\in[-2, 2]\times[-2, 2]$ into 4×10^4 squares.

Dropping the function $G(x, \eta, \hbar)$ in (2.6) is equivalent to approximating the full quantum map by the classical *stochastic* map

$$\begin{aligned} x_{n+1} &= f(x_n) - b\, y_n + \xi_n \\ y_{n+1} &= x_n + \eta_n \end{aligned} \tag{5.1}$$

with Gaussian δ-correlated noise sources ξ_n, η_n of intensity

$$\begin{aligned} \langle \xi_n \xi_m \rangle &= \hbar Q \delta_{nm} \\ \langle \eta_n \eta_m \rangle &= \frac{\hbar Q}{b} \delta_{nm} \\ \langle \xi_n \eta_m \rangle &= 0. \end{aligned} \tag{5.2}$$

In fact, (5.1), (5.2) can be obtained as the quasi-classical limit of an exact representation of the full quantum map (2.5), (2.6) by a quasi-stochastic map which has been introduced in [7]. The representation (5.1), (5.2) opens up the possibility to generate the steady state distribution of x, y directly by a stochastic simulation, i.e. by a procedure completely different and independent from the method used to generate Fig. 9. The result of such a stochastic simulation for $\hbar=0.001$ and the same partitioning as used in Fig. 9 is shown in Fig. 10. This figure is based on 10^7 iterations of the stochastic map. The agreement is reasonable, but we remark that in practice the stochastic simulation converges quite slowly to a smooth distribution, and

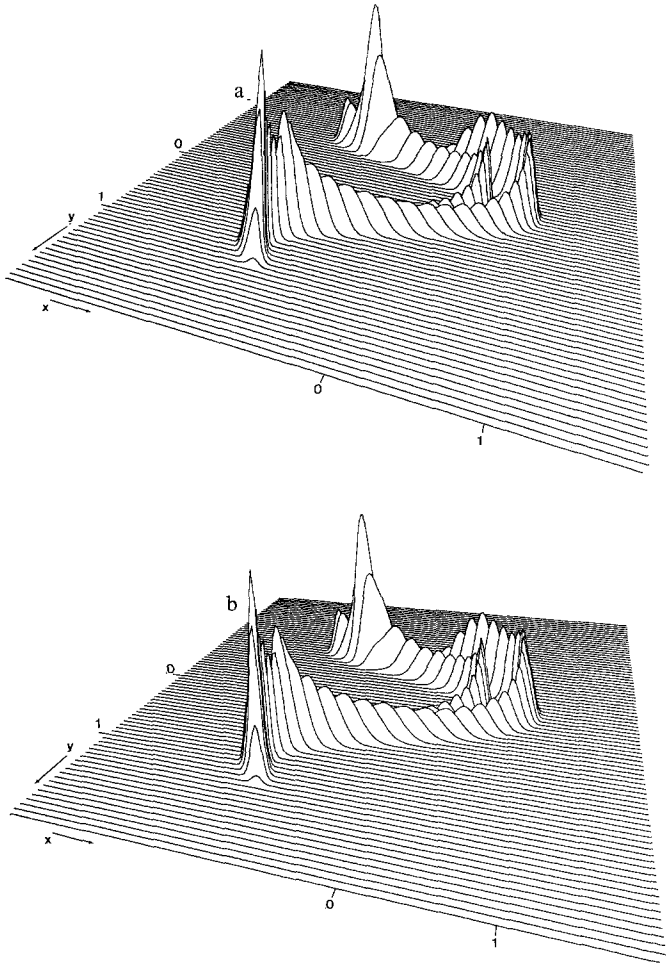

Fig. 9a and b. Stationary Wigner distribution (40 iterations) (**a**) and its approximation by Gaussian quantum noise for $a=3.4$, $b=0.3$, $\hbar=0.001$

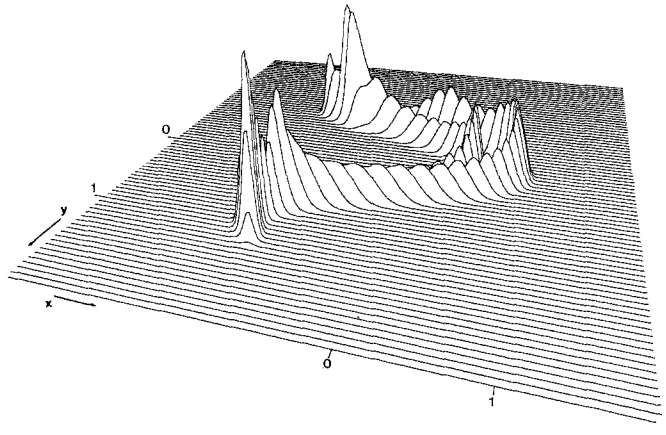

Fig. 10. Distribution obtained from 10^7 iterations of the stochastic map (5.1), (5.2) for $a=3.4$, $b=0.3$, $\hbar=0.001$

the computation time involved is larger by an order of magnitude compared to the method used to generate Fig. 9. On the other hand the stochastic approach is very direct and requires little extra thought.

6. Lowest lying non-vanishing eigenvalue of the master equation

The master equation in the form (2.5) allows for a separation of the n-dependence by the ansatz

$$W_n(x, y) = \sum_\lambda P_\lambda(x, y)\, e^{-\lambda n} \tag{6.1}$$

where the eigenfunctions P_λ satisfy the eigenvalue problem

$$e^{-\lambda} P_\lambda(x, y) = \int dx'\, dy'\, K(x, y; x', y')\, P_\lambda(x', y') \tag{6.2}$$

The stationary distribution $W_\infty(x, y)$ corresponds to the eigenvalue $\lambda = 0$

$$W_\infty(x, y) = P_0(x, y) \tag{6.3}$$

We note that

$$\int P_\lambda(x, y)\, dx\, dx = \delta_{\lambda, 0}. \tag{6.4}$$

The 'lowest lying' eigenvalues (i.e. those with the smallest non-vanishing real part) and the corresponding eigenfunctions determine the long-time behavior of the relaxation towards the steady state, as is evident from (6.1). These lowest lying eigenvalues and eigenfunctions can also be determined by iterations of the map (2.5), but now starting with initial quasi-probability functions in the subspace orthogonal to the steady state distribution, the orthogonality condition being

$$\int W_0(x, y)\, dx\, dx = 0. \tag{6.5}$$

By (6.1) such an initial distribution converges to a linear combinaton of the eigenfunctions corresponding to the lowest lying eigenvalues. In Fig. 11a–d we display the 18th to 21st iterates of an arbitrarily picked initial distribution satisfying (6.5). For this example the same parameter values and approximations as those underlying Fig. 8 were chosen. The iterates shown in Fig. 11b–d are magnified by a factor 2 compared to Fig. 11a, for clarity. It turns out that Fig. 11d, after appropriate rescaling, reproduces Fig. 11a quite accurately. Therefore, the imaginary part of the lowest lying eigenvalue λ is close to $\pm 2\pi/3$

$$\mathrm{Im}\,\lambda = \pm 2\pi/3 \tag{6.6}$$

corresponding to the fact, already mentioned above, that the system is close to the bifurcation into a 3-

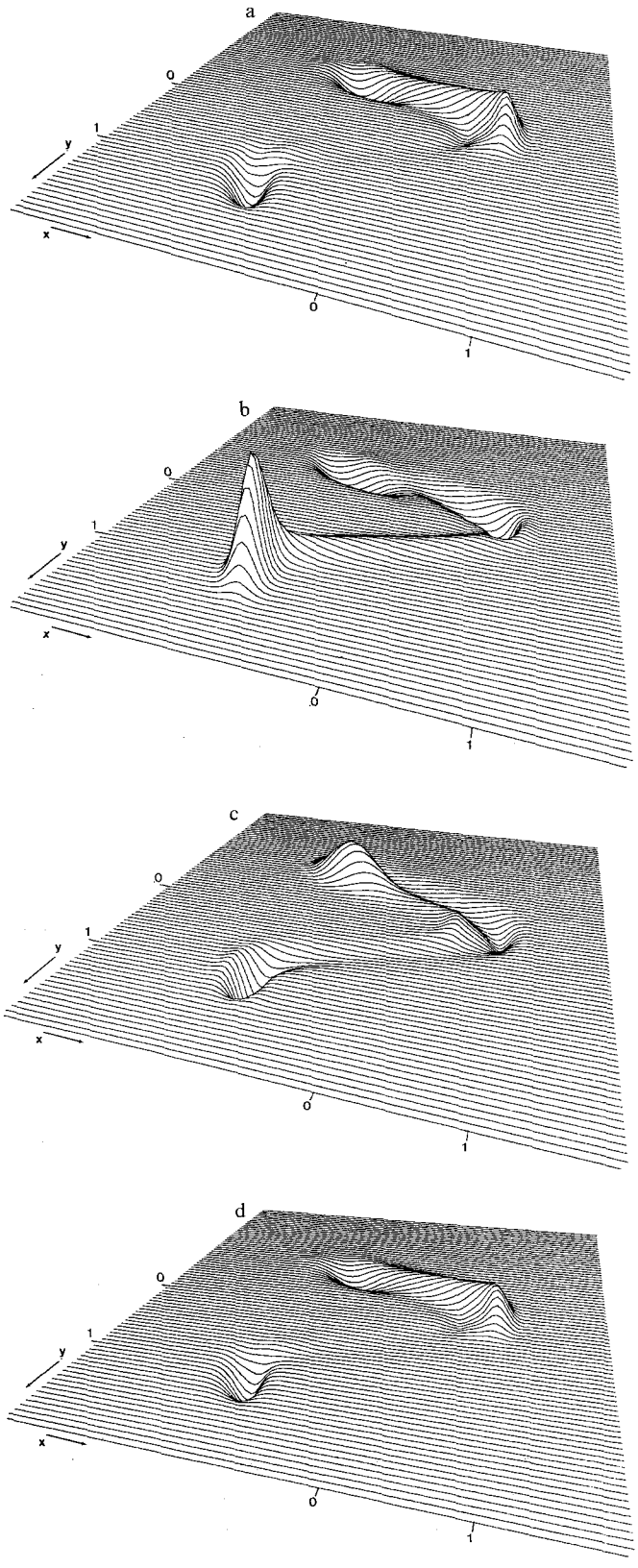

Fig. 11a–d. Linear combination of the two complex conjugate lowest lying eigenfunctions (**a**) and its next 3 iterates (**b–d**) for $a = 3.4$, $b = 0.3$, $\hbar = 0.01$

cycle. The real part of λ can be obtained from the scale factor S by which the distribution shown in Fig. 11d differs from that of Fig. 11a via

$$\mathrm{Re}\,\lambda = \tfrac{1}{3}|\ln S|. \tag{6.7}$$

Numerically, we calculate S from

$$S = \frac{1}{N}\sum_{i=1}^{N}\frac{W_{n+3}(x_i, y_i)}{W_n(x_i, y_i)} \tag{6.8}$$

and find from (6.7)

$$\mathrm{Re}\,\lambda \simeq 0.288 \tag{6.9}$$

for the parameter values chosen in this example. This value is in agreement with the fact that about 4 iterations are necessary to reach the steady state. We note, however, that $\mathrm{Re}\,\lambda$ is much smaller than the basic rate constant $|\ln b| \simeq 1.2$ which one infers from the contraction rate $b=0.3$ of the classical map, which shows that the proximity to a bifurcation point already leads to a considerable slowing down of the relaxation to the steady state.

7. Wigner distribution in the period doubling regime

Finally, we consider stationary solutions of the master Eq. (2.5), (2.10) in the period doubling regime of parameter space. Figure 12 shows cycles of the classical map (2.1) obtained for increasing values of a at fixed $b=0.3$. The figure makes clear, how the classical attractor of Fig. 2 is gradually built up for increasing

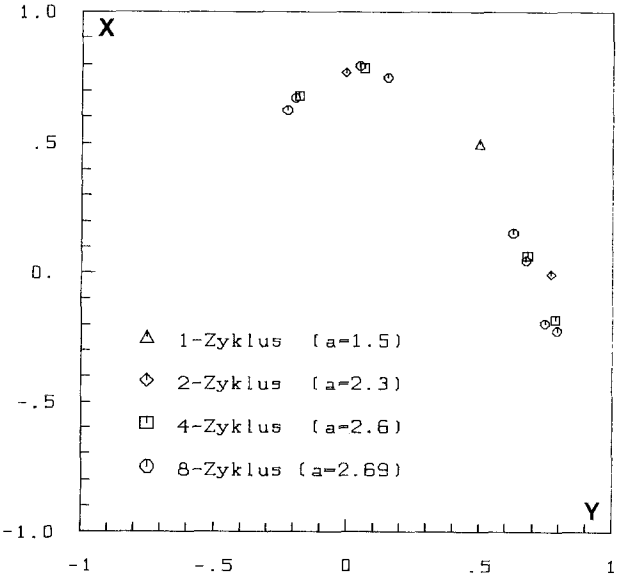

Fig. 12. Cycles of the classical map (2.1), (2.2) for $b=0.3$

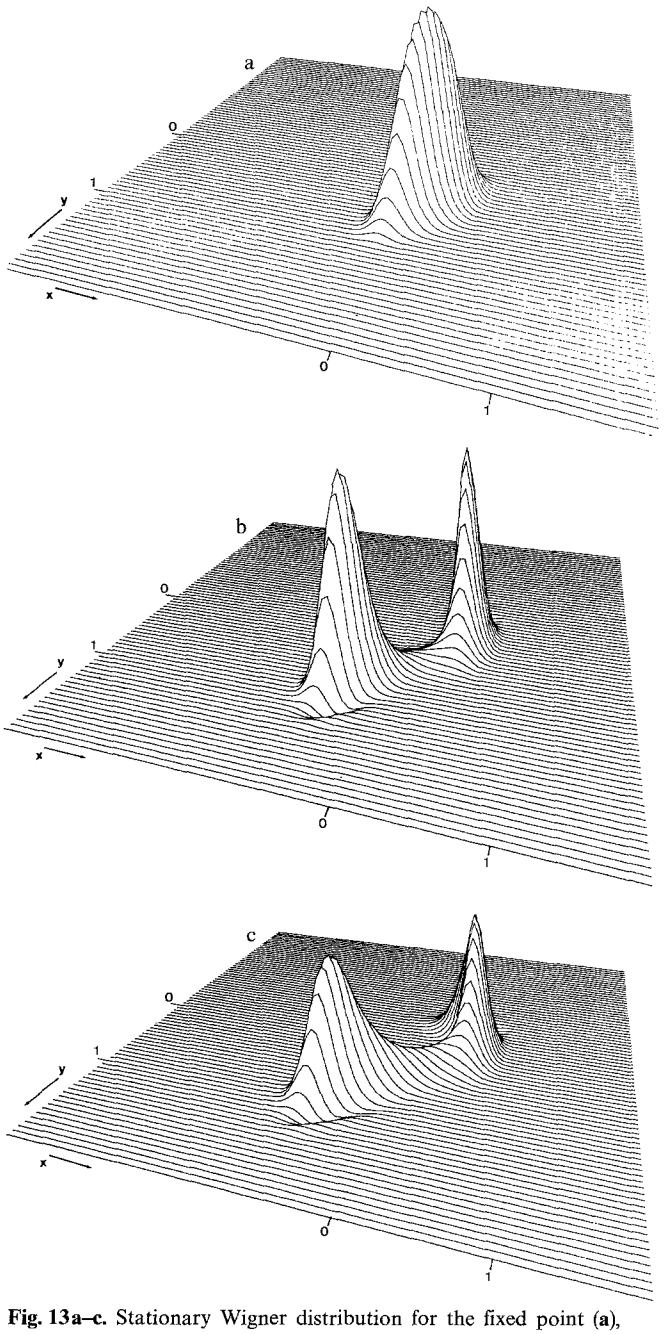

Fig. 13a–c. Stationary Wigner distribution for the fixed point (**a**), two cycle (**b**), and four-cycle (**c**) shown in Fig. 12. The four-cycle is not resolved

cycle length. In Fig. 13a–c the stationary Wigner distributions for the fixed point, two-cycle and four-cycle shown in Fig. 12 are given for the case $\hbar=0.01$ and using a grid of 10^4 squares in the interval $[-2,2] \times [-2,2]$. Obviously the 4-cycle cannot be resolved, and this remains true even if the effective $\hbar$ is decreased to 10^{-3}. As was shown in Sect. 5, in this latter case the stochastic approximation of the quantum map is already quantitatively valid. Figure 14 gives

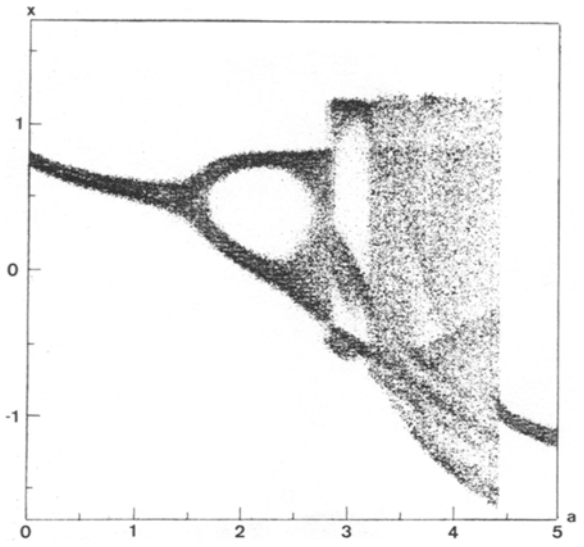

Fig. 14. Bifurcation diagram of the stochastic map (5.1), (5.2) for $b=0.3$, $\hbar=0.001$

the bifurcation diagram, obtained like Fig. 1, of the corresponding stochastic map (5.1), (5.2) with $\hbar = 10^{-3}$, which also shows that only the two cycle can be resolved in this case. According to scaling theories of noise in classical maps [7, 8], which, as we have shown above, are applicable in this case, the effective $\hbar$ would have to be decreased to $\simeq 10^{-6}$ in order to resolve the 4-cycle.

We would like to thank Michael Dörfle for useful suggestions concerning the numerical work.

References

1. Casati, G. (ed.): Chaotic behavior in quantum systems, theory and applications. New York: Plenum Press 1985;
Procaccia, I. (ed.): Chaos and related nonlinear phenomena; where do go from here?. New York: Plenum Pres 1987
2. Graham, R., Tél, T.: Z. Phys. B – Condensed Matter **60**, 127 (1985)
3. Hénon, M.: Comm. Math. Phys. **50**, 69 (1976)
4. Dittrich, Th., Graham, R.: Z. Phys. B – Condensed Matter **62**, 515 (1986)
5. Dittrich, Th., Graham, R.: Europhys. Lett. **3**, 259 (1987)
6. Graham, R.: Phys. Scr. **35**, 111 (1987)
7. Graham, R.: Europhys. Lett. **3**, 259 (1987)
8. Crutchfield, J.P., Farmer, J.D., Huberman, B.A.: Phys. Rep. **92**, 45 (1982)

R. Graham, S. Isermann
Fachbereich Physik
Universität – Gesamthochschule Essen
Postfach 103764
D-4300 Essen 1
Federal Republic of Germany

T. Tél
Institute for Theoretical Physics
Eötvös University
Budapest
Hungary